

# Performance of monolayer graphene nanomechanical resonators with electrical readout

Changyao Chen<sup>1†</sup>, Sami Rosenblatt<sup>2†</sup>, Kirill I. Bolotin<sup>3</sup>, William Kalb<sup>1</sup>, Philip Kim<sup>3</sup>, Ioannis Kyriassis<sup>2</sup>, Horst L. Stormer<sup>3,4,5</sup>, Tony F. Heinz<sup>2,3</sup> and James Hone<sup>1\*</sup>

**The enormous stiffness and low density of graphene make it an ideal material for nanoelectromechanical applications. Here, we demonstrate the fabrication and electrical readout of monolayer graphene resonators, and test their response to changes in mass and temperature. The devices show resonances in the megahertz range, and the strong dependence of resonant frequency on applied gate voltage can be fitted to a membrane model to yield the mass density and built-in strain of the graphene. Following the removal and addition of mass, changes in both density and strain are observed, indicating that adsorbates impart tension to the graphene. On cooling, the frequency increases, and the shift rate can be used to measure the unusual negative thermal expansion coefficient of graphene. The quality factor increases with decreasing temperature, reaching  $\sim 1 \times 10^4$  at 5 K. By establishing many of the basic attributes of monolayer graphene resonators, the groundwork for applications of these devices, including high-sensitivity mass detectors, is put in place.**

Since its discovery in 2004 (ref. 1), graphene has attracted attention because of its unusual two-dimensional structure and potential for applications<sup>2–4</sup>. Owing to its exceptional mechanical properties<sup>5</sup> and low mass density, graphene is an ideal material for use in nanoelectromechanical systems (NEMS), which are of great interest both for fundamental studies of mechanics at the nanoscale and for a variety of applications, including force<sup>6</sup>, position<sup>7</sup> and mass<sup>8</sup> sensing. Recent studies using optical and scanned probe detection have shown that micrometre-size graphene flakes can act as NEMS resonators in the megahertz range<sup>9,10</sup>. Electrical readout of these devices is important for integration, and is attractive for many applications. In addition, characterization of the basic attributes of these devices, including their response to applied voltage, added mass and changes in temperature, allows detailed modelling of their behaviour, which is crucial for rational device design.

Samples were fabricated by first locating monolayer graphene flakes on Si/SiO<sub>2</sub> substrates, then patterning metal electrodes and etching away the SiO<sub>2</sub> to yield suspended graphene. The ability to select monolayers in advance allows the control of device properties and facilitates electrical readout. The fabrication method also provides control over the lateral dimensions; devices can be generated as micrometre-wide sheets (Fig. 1a) or as lithographically defined nanoribbons (Fig. 1b). Because the etchant diffuses freely under the sheets, the SiO<sub>2</sub> is removed at the same rate everywhere under the graphene, so that the distance between the substrate and the suspended sheet is constant ( $\sim 100$  nm) across each device. For the same reason, the portion of each electrode that contacts the graphene is also suspended<sup>11,12</sup>, as depicted in Fig. 1c.

Following previous work<sup>13–15</sup>, we implemented an all-electrical high-frequency mixing approach (Fig. 1d) to the actuation and detection of mechanical resonances. A d.c. gate voltage  $V_g$  applied static tension to the device, an r.f. gate voltage with amplitude  $\delta V_g^f$  at frequency  $f$  was used to drive the motion, while a second r.f. voltage, at a slightly offset frequency  $f + \Delta f$ , was applied to the source. Because the graphene conductance changes with distance

from the gate, motion is detected as a mixed-down current  $I^{\Delta f}$  at the difference frequency  $\Delta f$ . The weaker gate response of the conductivity of multilayer graphene makes the use of monolayers advantageous for this method.

Figure 2a shows  $I^{\Delta f}$  as a function of drive frequency for a 3- $\mu\text{m}$ -wide, 1.1- $\mu\text{m}$ -long monolayer graphene resonator (device 1) at  $V_g = -7$  V, measured at room temperature. A prominent peak is observed near 65 MHz, which we interpret as the mechanical resonance of the graphene. Smaller peaks, which we assign to the resonance of the under-etched gold electrodes, appear near 20 and 25 MHz. The inset shows the same graphene resonance driven at a lower amplitude and fit to a Lorentzian lineshape. The width of the resonance corresponds to a quality factor  $Q = 125$ . This value is typical for the devices (more than 20) studied so far, and is consistent with previous results<sup>9</sup>.

The evolution of the resonances with  $V_g$  and device geometry supports the assignment of the two modes given above. The graphene resonance (Fig. 2b) is highly tunable, increasing in frequency away from a minimum near  $V_g = 0$  due to the tension induced by the gate voltage (the small observed shift of the resonant frequency minimum away from  $V_g = 0$  can be explained by trapped charges in the oxide and on the graphene<sup>13,14</sup>). On the other hand, the resonances of the much stiffer gold beams are, as expected, independent of gate voltage. The contrast between the two resonances serves to emphasize that the combination of high frequency and high tunability with an electrostatic gate is a unique feature of devices with thickness near the atomic scale such as graphene and single-walled carbon nanotubes<sup>14</sup>; it is seen in neither multilayer graphene<sup>9</sup> nor in NEMS resonators fabricated using top-down techniques. For devices with suspended graphene lengths  $L$  from  $\sim 0.5$  to 2  $\mu\text{m}$ , the graphene resonant frequency scales approximately as  $(1/L)$ , as expected for a thin membrane (see Supplementary Information). The resonant frequency of the gold, on the other hand, scales approximately as  $t/L_{\text{gold}}^2$ , where  $t$  is the electrode thickness and  $L_{\text{gold}}$  is the length of the suspended section of the gold electrode ( $\sim$ width of the graphene sheet), as expected for a thick beam.

<sup>1</sup>Department of Mechanical Engineering, Columbia University, New York 10027, USA, <sup>2</sup>Department of Electrical Engineering, Columbia University, New York 10027, USA, <sup>3</sup>Department of Physics, Columbia University, New York 10027, USA, <sup>4</sup>Department of Applied Physics, Columbia University, New York 10027, USA, <sup>5</sup>Bell Labs, Alcatel-Lucent, Murray Hill, New Jersey 07974, USA; <sup>†</sup>These authors contributed equally to this work. \*e-mail: jh2228@columbia.edu

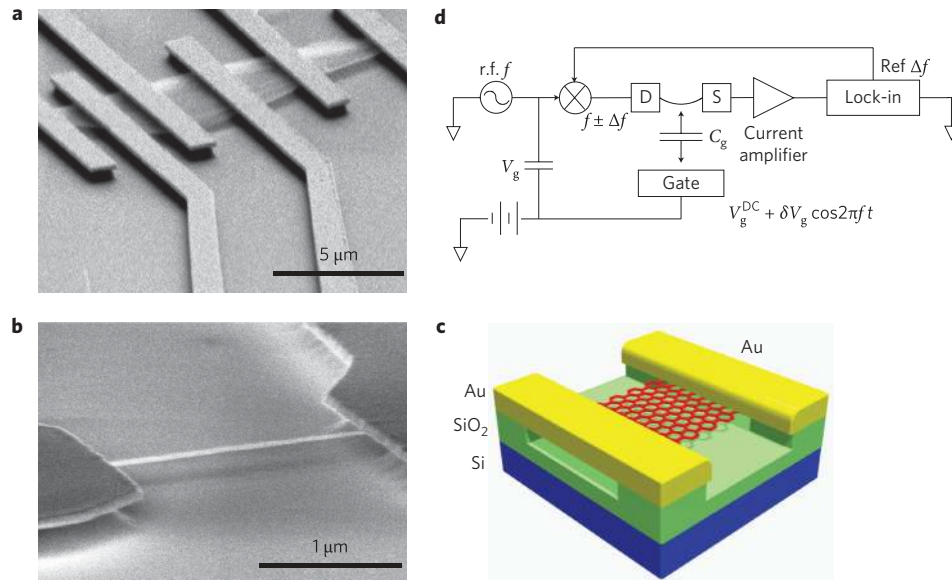


**Figure 1 | Device and experimental setup.** **a**, Scanning electron microscope (SEM) image of several resonators made from single-monolayer graphene flake. **b**, SEM image of suspended graphene nanoribbon, lithographically patterned to a width of 200 nm before suspension. **c**, Schematic of suspended graphene. The SiO<sub>2</sub> under the entire graphene flake is etched evenly, including the contact region. **d**, Diagram of electronic circuit. A carrier r.f. signal  $\delta V_{\text{sd}}^{f \pm \Delta f}$  is applied to the drain, and an r.f. drive signal  $\delta V_g^f$  together with d.c. bias  $V_g$  is applied to the gate. The current through the graphene is detected by a lock-in amplifier after pre-amplification, at an intermediate frequency  $\Delta f$  of 1 kHz.

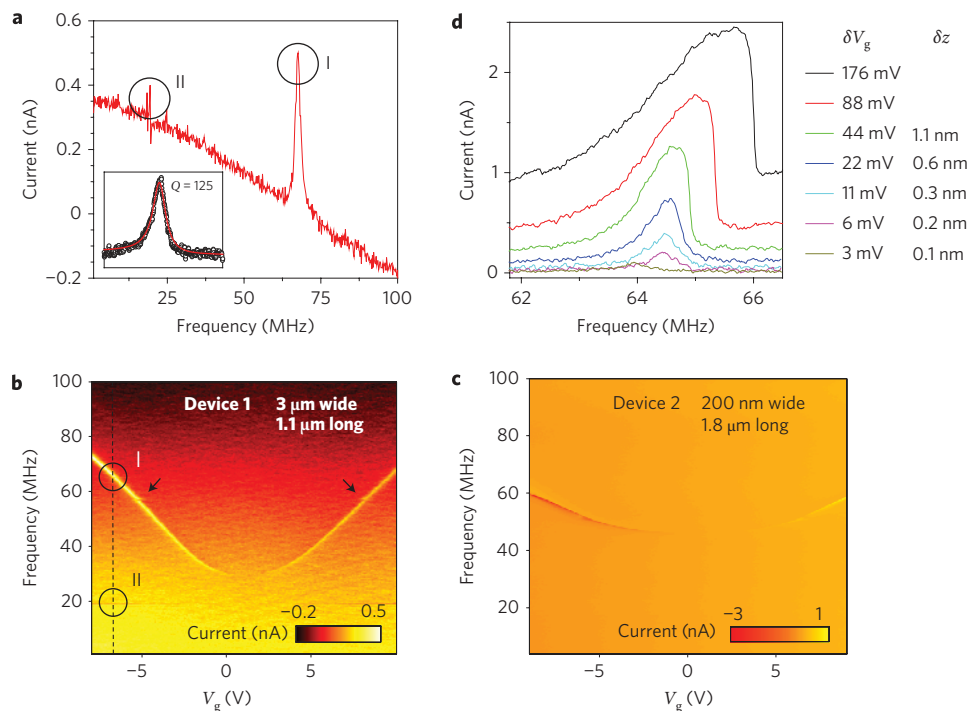


**Figure 2 | NEMS properties of graphene resonators.** **a**, Mixed-down current  $\delta I^{\Delta f}$  versus frequency for device 1 (3- $\mu\text{m}$  wide, 1.1- $\mu\text{m}$  long), taken at  $V_g = -7$  V from **b** (dashed black vertical line), with r.f. drive amplitude  $\delta V_g = 19$  mV and r.f. bias  $\delta V_{\text{sd}} = 110$  mV. The graphene resonance (I) appears at 65 MHz. Resonances of metal beams (II) are also visible below 25 MHz. Inset: the graphene resonance at low driving power, and Lorentzian fit (red line) with  $Q = 125$ . **b, c**,  $\delta I^{\Delta f}$  in colour scale as a function of both driving frequency and d.c. gate voltage  $V_g$  for device 1 (**b**) and device 2 (**c**, 200 nm wide, 1.8  $\mu\text{m}$  long). The graphene resonances, visible as parabola-shaped features, are highly tunable with gate voltage for both devices. In **b**, besides graphene resonances (I), resonances from the metal clamps are observed, both as non-tunable modes (II) and as avoided crossing points (arrows). These modes are absent in device 2, which is much narrower. **d**,  $\delta I^{\Delta f}$  versus driving frequency for seven different drive amplitudes ( $\delta V_g$ ), with  $V_g = -7$  V,  $\delta V_{\text{sd}} = 7.5$  mV. The estimated vibration amplitudes ( $\delta z$ ) are given for each  $\delta V_g$  (see Supplementary Information). The onset of nonlinearity effects corresponds to  $\delta V_g = 44$  mV, with estimated vibration amplitude of 1.1 nm. Beyond this linear regime, the amplitude estimation is not valid.

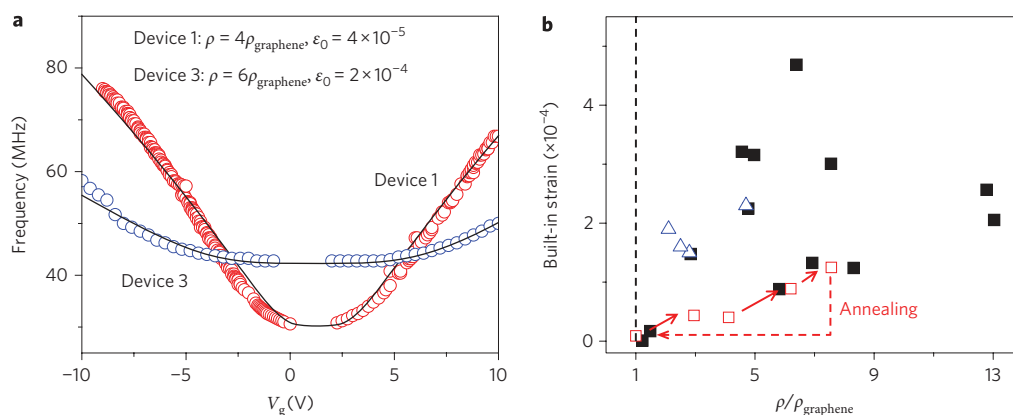


**Figure 3 | Modelling of device behaviour.** **a**, Measured resonant frequency versus  $V_g$  for two devices; solid lines are fits to a membrane model with the values of  $\rho$  and  $\epsilon_0$  shown. **b**, Built-in strain versus normalized mass density. The filled squares show data for 11 as-fabricated devices. The open triangles show data for the device cleaned by ohmic heating described in Fig. 4. The open squares show data for the pentacene deposition (red arrows) and the removal of pentacene (dashed red line) by the annealing process described in Fig. 5. The dashed black line shows the mass density of pristine graphene.

For narrow graphene ribbons, such as in Fig. 2c, the gold beam resonance occurs above the measured frequency range, and only the graphene resonance is observed.

The observation of the metal resonances by electromechanical mixing implies that the motion of the metal electrode is transferred to the graphene, because the conductance of the gold is independent of gate voltage. As expected, the coupling between the two resonant modes is strongest when the frequencies are similar. This behaviour is manifested in many devices as avoided crossings at intersections between the metal and graphene modes, as indicated by the arrows in Fig. 2a (and appearing more prominently in other devices, such as shown in Figs 4 and 5). In addition to being of fundamental interest as a coupled nanoscale–microscale system, these resonances demonstrate that graphene can be used to transduce the motion of larger resonant systems with minimal damping.

Figure 2d shows the evolution of graphene resonance (for device 1) with drive amplitude. As  $\delta V_g$  increases, the peak grows in height, shifts upwards in frequency, and changes from a symmetric Lorentzian to an asymmetric shape characteristic of a nonlinear response. Above a drive amplitude of  $\sim 44$  mV, corresponding to an oscillation amplitude of  $\sim 1.1$  nm, the resonance develops bistable behaviour<sup>14</sup> (see Supplementary Information). The ratio of the amplitude at the onset of nonlinearity to the noise floor gives a dynamic range<sup>16</sup> of  $\sim 60$  dB. Importantly for applications of these devices, the measured peak current values are approximately two orders of magnitude larger than those observed in carbon nanotubes for the same applied power at room temperature<sup>14,17</sup>. This improvement in signal levels is a direct consequence of the ability to fabricate micrometre-wide devices with higher conductance than that of a one-dimensional nanotube.

### Mechanical modelling

Modelling the behaviour of the graphene resonators is crucial for device design and interpretation of experimental results. We use a continuum model that treats the graphene resonators as membranes with zero bending stiffness<sup>5,18–20</sup> (see Supplementary Information). In this model, the resonant frequency is given by

$$f_{\text{res}}(V_g) = \frac{1}{2L} \sqrt{\frac{T_0 + T_e(V_g)}{\rho w}} \quad (1)$$

where  $L$  and  $w$  are the length and width of the graphene sheet, respectively. The two-dimensional mass density  $\rho$  represents the sum of the contributions from the graphene and any adsorbates, and therefore in general  $\rho \geq \rho_{\text{graphene}} = 7.4 \times 10^{-19} \text{ g } \mu\text{m}^{-2}$ .

Near  $V_g = 0$ , the frequency is set by the built-in tension  $T_0$  and  $\rho$ , whereas at higher  $V_g$  the electrostatically induced tension  $T_e$  causes the frequency to increase roughly as  $V_g^{2/3}$ . The model successfully describes the gate voltage dependence of the resonant frequency in all of the  $>20$  devices studied so far (with lengths from  $\sim 0.5$  to  $2 \mu\text{m}$  and widths from  $0.2$  to  $2 \mu\text{m}$ ); two representative curves are shown in Fig. 3a. Furthermore, it can be used to deduce both the mass density and the built-in tension in the graphene sheet, which are left as fitting parameters. The solid black points in Fig. 3b show the built-in tension (converted to strain using the measured stiffness of graphene<sup>5</sup> in order to normalize for the geometry) and density (normalized to the density of a graphene sheet) for 11 devices, as derived from the curve fitting. In all cases, a density larger than that of pristine graphene is required to fit the observed data. We attribute this extra mass to electron-beam resist (poly(methyl methacrylate), PMMA) residue from the fabrication process<sup>21,22</sup>. The built-in strain is positive, and of order  $10^{-4}$  in all of the as-fabricated devices, which accounts for the observed large resonant frequencies even near  $V_g = 0$ . Although there is considerable scatter in the data, we observe that the built-in strain is generally larger in devices with more adsorbed residue, which suggests that the PMMA tends to impart a tension to the graphene.

The measured strain can also be used to predict the amplitude at the onset of nonlinearity  $a_c$ . By modifying an expression previously derived for beams<sup>23</sup> we obtain, for a membrane,

$$a_c = 0.56L \sqrt{\frac{\epsilon}{Q}} \quad (2)$$

where  $\epsilon$  is the strain of the resonator. For the device studied in Fig. 2d, this expression gives  $a_c = 1.5$  nm, very close to the measured value.

The validity of the continuum model is further supported by two experiments described below. In the first, a calibrated mass is added to the resonator, whereas the second uses thermal contraction to change only the tension. In both cases, the model correctly predicts the change in resonator mass.

### Response to changes in mass

Ohmic heating of suspended graphene in vacuum has previously been shown to significantly improve its electronic mobility<sup>11,21</sup>, presumably through the desorption of residue from the graphene surface. The ability to directly measure the mass of graphene resonators provides a tool to monitor this process, and to correlate

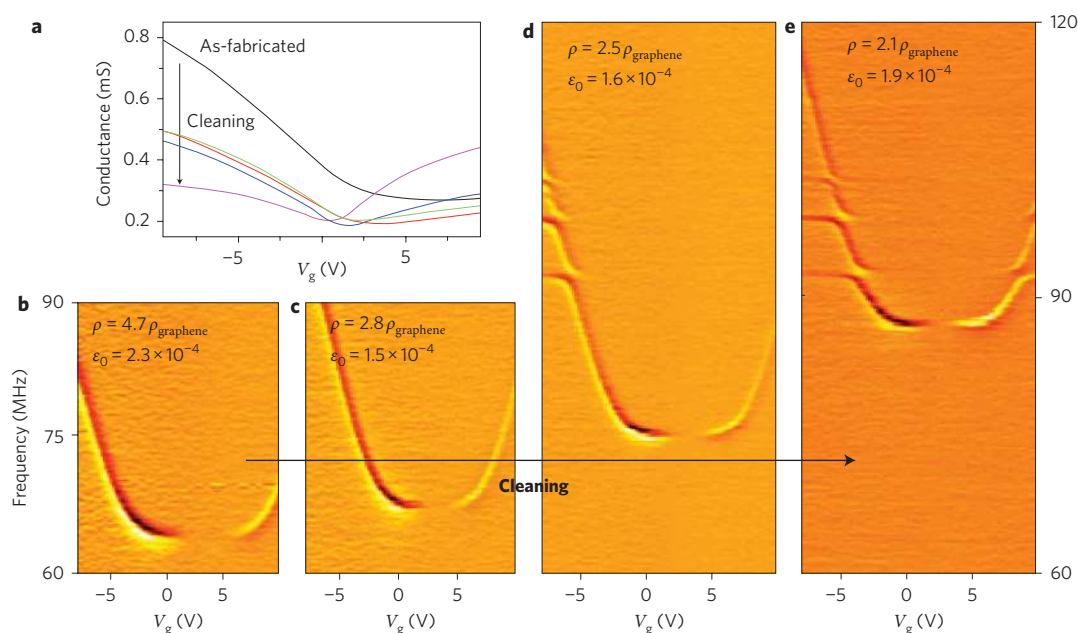


**Figure 4 | Removal of mass by ohmic heating.** **a**, Room-temperature conductance ( $V_{sd} = 1$  mV) versus gate voltage for a device before (black curve) and after ohmic-heating cycles to  $V_{sd} = 1.5$  V (red), 1.6 V (green), 1.8 V (blue) and 3 V (pink). Successive curves show decreased conductance at negative gate voltage (black arrow), increased conductance at positive gate voltage, and conductance minima closer to zero gate voltage. **b–e**, Resonant response (frequency versus gate voltage plotted as a derivative with a colour scale), for the as-fabricated device (**b**), and after annealing at 1.5 V (**c**), 1.6 V (**d**) and 1.8 V (**e**). The derived strain and density for each step are shown, and confirm that residue is removed. Because of damage to the device, it was not possible to obtain a resonance curve after the 3 V annealing step.

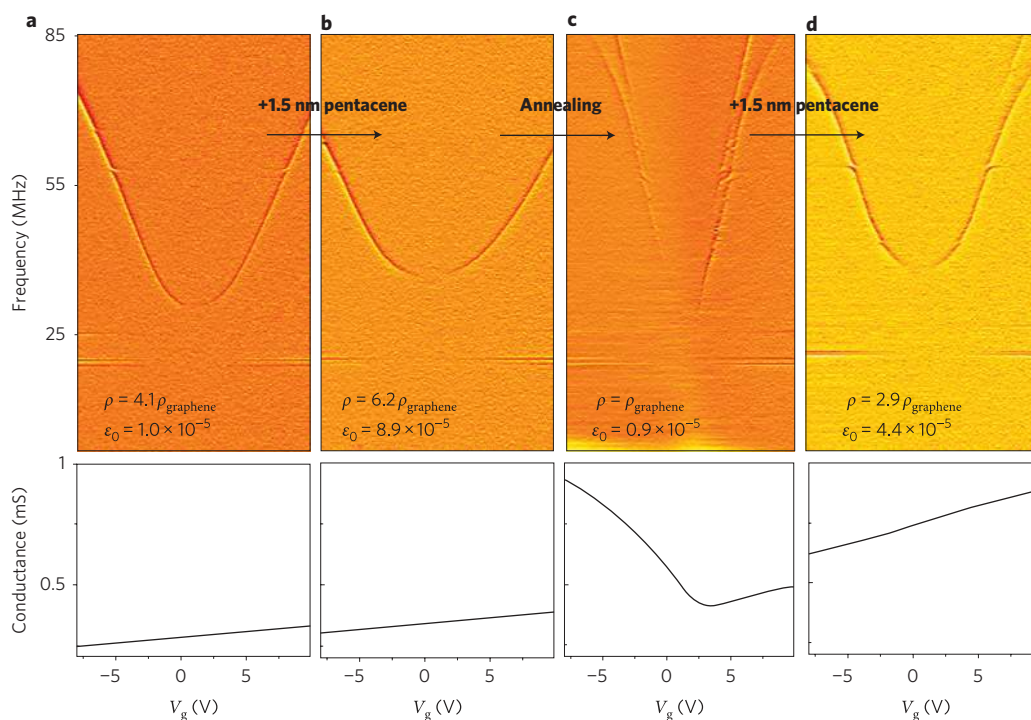


**Figure 5 | Effects of mass loading.** **a**, Resonant response (frequency versus gate voltage plotted as a derivative with a colour scale) for an as-fabricated device. **b–d**, Response of the same device after evaporation of 1.5 nm pentacene (**b**), after cleaning by ohmic heating (**c**) and after deposition of another 1.5 nm of pentacene (**d**). The derived strain and density for each step are shown. Bottom panels show the d.c. conductance as function of  $V_g$  for each step.

electrical performance with the amount of residue. Figure 4a shows the conductance of the graphene resonator as a function of gate voltage, measured after each of four successive ohmic heating steps. At each step, the conductance minimum (the charge

neutrality point) moves closer to  $V_g = 0$ , and the n-branch conductance increases while the p-branch decreases. Figure 4b–e shows the resonant frequency as a function of gate voltage for the same device, in the as-fabricated state (Fig. 4b), and after each of the first three



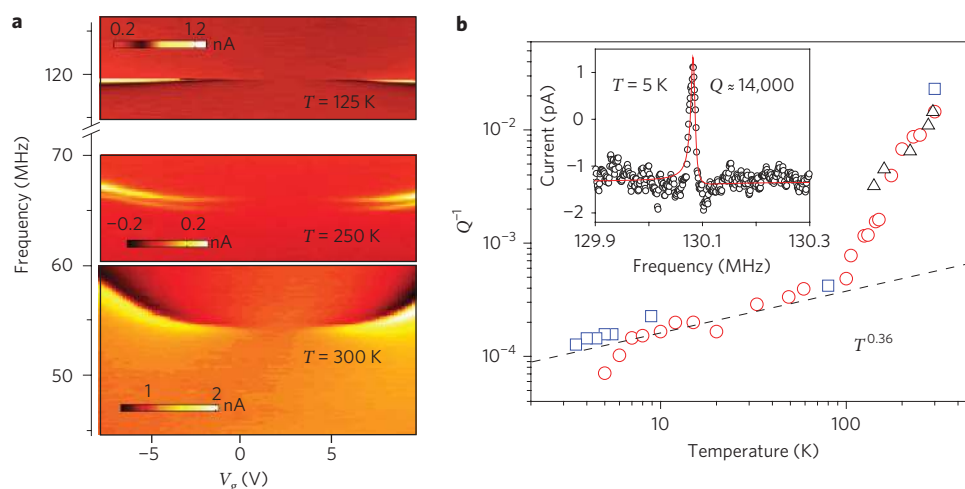


**Figure 6 | Temperature dependence.** **a**, Resonant response (frequency versus gate voltage plotted as a current with a colour scale) at different temperatures, showing an upshift of resonances and decreasing tunability. The origin of the peak splitting at 250 K is not clear. **b**, Temperature dependence of energy dissipation ( $Q^{-1}$ ). Different symbols indicate data from different devices. One device (red circles) shows increasing resistance (up to  $\sim 1\text{ M}\Omega$ ) upon cooling whereas the others retain resistance in the  $\text{k}\Omega$  range. The dashed line shows  $T^{0.36}$  behaviour reported for similar measurements on carbon nanotubes<sup>30</sup>. Inset: resonant peak, showing a quality factor of 14,000 at 5 K.

heating steps (Fig. 4c–e). The resonant frequency shifts upwards at each step, consistent with a loss of mass; fitting the data to the membrane model shows that the two-dimensional density decreases monotonically, from 4.7 to 2.1 times that of graphene. The built-in strain in the sheet also changes slightly with each cleaning step. In this experiment, the device was damaged after the fourth step, preventing full removal of the PMMA residue. The room-temperature quality factor did not change appreciably during the entire process.

We next tested the response of a resonator to the addition of a known amount of mass. This was accomplished by evaporating pentacene<sup>24</sup> onto the device in a vacuum chamber, while measuring the device response *in situ*. The added mass was calibrated by a quartz crystal microbalance (QCM). Figure 5a shows the resonant frequency as a function of gate voltage for the as-fabricated device, which is again fit to yield the density and strain. The charge neutrality point is located at  $V_g < -10\text{ V}$ . Figure 5b shows the corresponding data after deposition of 1.5 nm of pentacene. At high  $|V_g|$ , where there is a large gate-induced tension, the added mass results in the expected decrease in the resonant frequency. At low  $|V_g|$ , however, the resonant frequency upshifts, indicating that the added pentacene increases the built-in strain. Similar behaviour is observed after a second 1.5-nm evaporation step (not shown). The graphene was then ohmically heated to remove the adsorbed material. After cleaning (Fig. 5c), the resonant frequency shifts downward at low  $|V_g|$  and shifts dramatically upward at high  $|V_g|$ , consistent with a decrease in both the mass and the built-in tension. An additional mode, the nature of which is uncertain, is also seen, and the charge neutrality point is observable in the measured  $V_g$  range. Finally, 1.5 nm of pentacene is again evaporated on the clean device (Fig. 5d). Once again, the frequency shifts downward at high  $|V_g|$  and upwards at low  $|V_g|$ , and the charge neutrality point moves to the left. This result suggests the possibility of using graphene resonators as multifunctional sensors by simultaneously tracking the resonant frequency and the charge neutrality point displacement<sup>2</sup>. The use of ohmic heating to regenerate the devices is also shown to be possible, although the process seems to damage the sheet in some cases. Improvements to the cleaning process may be needed to minimize the damage and extend the device lifetime. As expected, the gate-independent metal resonances remain largely unchanged during the entire process.

From the continuum model, the sheet mass density is found to increase after each evaporation step by an amount equivalent to 1.5 nm of pentacene, in agreement with the thickness measured by the QCM. This provides strong confirmation of the model. In addition, in this device, ohmic heating is sufficient to remove essentially all of the residue, yielding a density close to that of pristine graphene (Fig. 5c). Also, the built-in strain increases with the thickness of the adsorbed layer (Fig. 3b), indicating that adsorbates can impart a tension to the suspended graphene sheet.

In analysing the mass response of NEMS devices, one typically assumes that mass loading does not change the mechanics of the device. The frequency shift<sup>16</sup> is then simply  $(\Delta f/f) \approx -(1/2)(\Delta m/m)$ . An important result of this study is that the response of atomically thin resonators is not so simple, because the interaction between adsorbates and the sheet must also be considered. For instance, adsorbed mass can even shift the resonance upwards in frequency when the tension is small, as is observed in our devices near  $V_g = 0$ . Using devices with large built-in tension should minimize the effects of this interaction. Alternatively, it may be possible to use this effect to discriminate between different types of adsorbates by the tension they impart to the sheet.

### Low-temperature behaviour

To explore further the performance of the graphene resonators, we studied their behaviour as a function of temperature. Upon cooling, the resonant frequency shifts upwards, and its tunability with  $V_g$  decreases (Fig. 6a). This behaviour is a result of the geometry of our devices: when the temperature decreases, the suspended metal electrodes contract isotropically (see Supplementary Information), imparting tension to the graphene sheet. The frequency shifts are consistently observed in the four devices measured to date at low temperature, and are fully reversible upon warming, indicating that no slipping occurs between the graphene and the metal electrodes. The large temperature response shows the potential of using thermal effects for frequency tuning<sup>25</sup>, or for direct drive of the resonance<sup>26</sup>. The built-in strain measured using the continuum model increases upon cooling, from  $4.7 \times 10^{-4}$  at 295 K to  $6.9 \times 10^{-4}$  at 250 K. The mass density of the resonator, on the other hand, remains essentially constant ( $6.4\rho_{\text{graphene}}$ ), as expected. At lower temperatures, the lack of measurable tunability prevents independent determination of both density and strain. However, the strain can be

determined by using the density obtained at higher temperatures. At 125 K, for instance, the strain is found to be  $2.3 \times 10^{-3}$ .

For practical use in MEMS/NEMS devices and other applications, accurate measurement of thermal expansion is important to enable modelling of thermal effects. In addition, this effect is of fundamental interest in graphene: as a two-dimensional material, it possesses an unusual negative thermal expansion coefficient due to out-of-plane vibrational modes<sup>27</sup>. We used a finite-element model to determine the shrinkage of the substrate and electrodes to infer the thermal expansion coefficient of the graphene from the measured strain. When bulk values for the thermal expansion coefficients of gold and silicon are used, the model predicts that cooling from 295 to 250 K should impart an additional strain  $\Delta\epsilon = 5.5 \times 10^{-4}$  to the graphene, which is larger than the observed increase. The difference is due to the negative thermal expansion coefficient of graphene, for which we derive a value  $\alpha_{\text{graphene}} = -7.4 \times 10^{-6} \text{ K}^{-1}$ . This is larger in magnitude than predicted theoretically<sup>28</sup>, but is in excellent agreement with recently reported experimental results<sup>29</sup>. The observed upshift of the resonant frequency of the gold electrodes is consistent with a value of the gold thermal expansion coefficient within 5% of the bulk value, and a derived  $\alpha_{\text{graphene}}$  within 6% of that calculated above. These results clearly demonstrate the utility of resonant techniques in measuring the thermal expansion of graphene and similar materials, and a more detailed study of this phenomenon is currently under way. In addition, note that, with suitable choice of sample and electrode geometry, the thermally induced frequency shifts in graphene resonators can be engineered to be positive, negative or zero.

In addition to the frequency shifts, an increase in the quality factor was observed with decreasing temperature. Figure 6b shows the temperature dependence of the dissipation  $Q^{-1}$  for three devices, as measured by fitting the resonance peaks to a Lorentzian function in the linear response regime. These devices have varying electrical properties and levels of residual PMMA, but all three show remarkably similar behaviour. Upon cooling from room temperature,  $Q^{-1}$  drops quickly (roughly as  $T^3$ ) and the quality factor reaches  $\sim 3,000$  at 100 K. Below this temperature, the dissipation decreases more slowly, roughly as  $T^{0.3-0.4}$ . The quality factor reaches  $\sim 1 \times 10^4$  at 5 K (inset of Fig. 6b). In this regime, both the temperature dependence and magnitude are remarkably close to those recently reported for ultraclean carbon nanotubes<sup>30</sup> at lower temperatures ( $Q \approx 1 \times 10^5$  at 0.01 K, and  $Q^{-1} \propto T^{0.36}$  and from 0.01 to 1 K). NEMS resonators made from nanocrystalline diamond<sup>31</sup> ( $T^{0.2}$ ), GaAs (ref. 32) ( $T^{0.25}$ ) and other bulk materials<sup>33</sup> also show similar temperature dependence at low  $T$ . In this study, samples of different sizes, electrical properties and cleanliness show nearly identical behaviour. The origin for this temperature dependence is still unknown.

## Conclusions

Using the measured response to mass loading and the observed dynamic range, we estimate the mass sensitivity of the best sample ( $Q = 14,000$  at low  $T$ ) to be  $\sim 2 \text{ zg}$ , with a detection bandwidth set by the lock-in amplifier integration time (300 ms). This is a somewhat larger mass than recently demonstrated using nanotubes<sup>34,35</sup>, but could be reduced by improving the noise performance of the electrical detection system. Compared to nanotubes, graphene resonators have the advantage of more reproducible electrical properties and a larger surface area for capture of the incoming mass flux. Because the electrical properties of graphene are sensitive to adsorbed species<sup>2</sup>, it should also be possible to achieve multifunctional devices that combine charge and mass sensing down to the single molecule level.

Compared to other materials commonly used for NEMS, graphene possesses an important and as-yet unexploited advantage: it can withstand ultrahigh strains, up to  $\sim 25\%$  in nanoindentation experiments<sup>5</sup> and  $\sim 3\text{--}5\%$  for micrometre-sized samples subjected

to uniaxial strain<sup>36,37</sup>. In top-down fabricated NEMS, high resonant frequencies are achieved by reducing the device dimensions. This size reduction reduces both the output signal magnitude and the amplitude at the onset of nonlinearity, decreasing the dynamic range and making gigahertz-range transduction difficult. Micrometre-scale graphene devices, subjected to strains of order 1%, should achieve gigahertz operation while maintaining the robust signal levels observed in this study. An additional advantage is that the amplitude at the onset of nonlinearity increases with strain (equation (2)), so that it should be possible to simultaneously increase the frequency and dynamic range (and therefore the mass sensitivity). It may be possible to achieve such large strains by integrating graphene with MEMS/NEMS structures.

## Methods

**Device fabrication.** Graphene flakes (Toshiba Ceramics) were deposited on a  $\text{SiO}_2/\text{Si}$  substrate by mechanical exfoliation, optically located by their contrast<sup>38</sup> and subsequently confirmed to be monolayers with Raman spectroscopy<sup>39</sup>. Metal electrodes (chromium/gold) were patterned on the graphene by electron-beam lithography. An optional second step of lithography and oxygen plasma etching could be used to shape the graphene after patterning of electrodes. The devices were then suspended by etching the  $\text{SiO}_2$  epilayer using buffered oxide etchant (BOE), followed by critical point drying to suspend the graphene between the electrodes<sup>11</sup>. We have found that BOE etches uniformly underneath the graphene layer, rather than isotropically from the edge as for most materials (K. I. Bolotin, unpublished). This permits suspension of devices with a uniform gap below the graphene, even for sheets with dimensions over  $1 \mu\text{m}$ . The resulting wide suspended graphene sheets are low-impedance devices, which is helpful in matching to high-frequency electronics. Lithographic control also allows narrow ribbon resonators<sup>40</sup>, as shown in Fig. 1b. The combination of optical thickness identification and lithographic patterning gives us full three-dimensional knowledge of the device geometry. Although the oxide layer below the graphene in the area covered by the electrode is removed in the etching process, the adhesion between graphene and metal still provides good mechanical clamping.

**Electromechanical mixing.** The method implemented here is derived from previous studies of carbon nanotube resonators<sup>14</sup>, with minor modifications (see Supplementary Information). The suspended graphene is actuated by the potential difference between the sheet and the silicon substrate (gate). A d.c. voltage  $V_g$  is applied to the gate electrode to adjust the tension in the sheet, and an r.f. voltage  $\delta V_g^f$  sets it into motion at frequency  $f$ . A second r.f. signal consisting of two equal-amplitude sidebands  $\delta V_{\text{sd}}^f \pm \Delta f$  is applied to the drain electrode, so that a mixed-down current appears across the device at the intermediate frequency  $\Delta f$  with amplitude

$$I^{\Delta f} = \frac{dG}{dV_g} \delta V_{\text{sd}}^f \pm \Delta f \left( \delta V_g^f + V_g \frac{\delta z^f}{z} \right) \quad (3)$$

where  $G = \delta I / \delta V_{\text{sd}}$  is the conductance of the sheet,  $\delta z^f$  is the amplitude of vibration at the driving frequency and  $z$  the graphene-substrate distance. The magnitude of this current depends on the modulation of the conductance with gate voltage  $dG/dV_g$ , and is detectable for drain and gate signals in the millivolt range. The conductance swing per micrometre width of graphene is typically  $>10 \mu\text{S V}^{-1}$  at room temperature, a consequence of the large contact area, low contact resistance and high mobility of monolayer graphene, and can be improved by increased gate efficiency<sup>41</sup>. The first term in parentheses is purely electronic and results in a smooth background, whereas the second term results from the mechanical vibration of the sheet and peaks at the resonant frequency. All the measurements are carried out in a vacuum chamber ( $<1 \times 10^{-5}$  torr).

Received 7 July 2009; accepted 13 August 2009;  
published online 20 September 2009

## References

- Novoselov, K. S. *et al.* Electric field effect in atomically thin carbon films. *Science* **306**, 666–669 (2004).
- Schedin, F. *et al.* Detection of individual gas molecules adsorbed on graphene. *Nature Mater.* **6**, 652–655 (2007).
- Mohanty, N. & Berry, V. Graphene-based single-bacterium resolution biodevice and DNA transistor: interfacing graphene derivatives with nanoscale and microscale biocomponents. *Nano Lett.* **8**, 4469–4476 (2008).
- Meric, I. *et al.* Current saturation in zero-bandgap, top-gated graphene field-effect transistors. *Nature Nanotech.* **3**, 654–659 (2008).
- Lee, C., Wei, X. D., Kysar, J. W. & Hone, J. Measurement of the elastic properties and intrinsic strength of monolayer graphene. *Science* **321**, 385–388 (2008).

6. Mamin, H. J. & Rugar, D. Sub-attoNewton force detection at millikelvin temperatures. *Appl. Phys. Lett.* **79**, 3358–3360 (2001).
7. LaHaye, M. D., Buu, O., Camarota, B. & Schwab, K. C. Approaching the quantum limit of a nanomechanical resonator. *Science* **304**, 74–77 (2004).
8. Yang, Y. T. *et al.* Zeptogram-scale nanomechanical mass sensing. *Nano Lett.* **6**, 583–586 (2006).
9. Bunch, J. S. *et al.* Electromechanical resonators from graphene sheets. *Science* **315**, 490–493 (2007).
10. Garcia-Sanchez, D. *et al.* Imaging mechanical vibrations in suspended graphene sheets. *Nano Lett.* **8**, 1399–1403 (2008).
11. Bolotin, K. I. *et al.* Ultrahigh electron mobility in suspended graphene. *Solid State Commun.* **146**, 351–355 (2008).
12. Stolyarova, E. *et al.* Observation of graphene bubbles and effective mass transport under graphene films. *Nano Lett.* **9**, 332–337 (2009).
13. Witkamp, B., Poot, M. & van der Zant, H. S. J. Bending-mode vibration of a suspended nanotube resonator. *Nano Lett.* **6**, 2904–2908 (2006).
14. Sazonova, V. *et al.* A tunable carbon nanotube electromechanical oscillator. *Nature* **431**, 284–287 (2004).
15. Knobel, R. G. & Cleland, A. N. Nanometre-scale displacement sensing using a single electron transistor. *Nature* **424**, 291–293 (2003).
16. Ekinici, K. L. & Roukes, M. L. Nanoelectromechanical systems. *Rev. Sci. Instrum.* **76**, 061101 (2005).
17. Lassagne, B., Garcia-Sanchez, D., Aguasca, A. & Bachtold, A. Ultrasensitive mass sensing with a nanotube electromechanical resonator. *Nano Lett.* **8**, 3735–3738 (2008).
18. Atalaya, J., Isacsson, A. & Kinaret, J. M. Continuum elastic modeling of graphene resonators. *Nano Lett.* **8**, 4196–4200 (2008).
19. Bunch, J. S. *et al.* Impermeable atomic membranes from graphene sheets. *Nano Lett.* **8**, 2458–2462 (2008).
20. Yakobson, B. I., Brabec, C. J. & Bernholc, J. Nanomechanics of carbon tubes: instabilities beyond linear response. *Phys. Rev. Lett.* **76**, 2511–2514 (1996).
21. Moser, J., Barreiro, A. & Bachtold, A. Current-induced cleaning of graphene. *Appl. Phys. Lett.* **91**, 163513 (2007).
22. Ishigami, M. *et al.* Atomic structure of graphene on SiO<sub>2</sub>. *Nano Lett.* **7**, 1643–1648 (2007).
23. Postma, H. W. C., Kozinsky, I., Husain, A. & Roukes, M. L. Dynamic range of nanotube- and nanowire-based electromechanical systems. *Appl. Phys. Lett.* **86**, 223105 (2005).
24. Dimitrakopoulos, C. D. & Malenfant, P. R. L. Organic thin film transistors for large area electronics. *Adv. Mater.* **14**, 99–117 (2002).
25. Jun, S. C. *et al.* Electrothermal tuning of Al-SiC nanomechanical resonators. *Nanotechnology* **17**, 1506–1511 (2006).
26. Bargatin, I., Kozinsky, I. & Roukes, M. L. Efficient electrothermal actuation of multiple modes of high-frequency nanoelectromechanical resonators. *Appl. Phys. Lett.* **90**, 093116 (2007).
27. Suleimanov, R. A. & Abdullaev, N. A. The nature of negative linear expansion of graphite crystals. *Carbon* **31**, 1011–1013 (1993).
28. Mounet, N. & Marzari, N. First-principles determination of the structural, vibrational and thermodynamic properties of diamond, graphite and derivatives. *Phys. Rev. B* **71**, 205214 (2005).
29. Bao, W. *et al.* Controlled ripple texturing of suspended graphene and ultrathin graphite membranes. *Nature Nanotech.* **4**, 562–566 (2009).
30. Huttel, A. *et al.* Carbon nanotubes as ultrahigh quality factor mechanical resonators. *Nano Lett.* **9**, 2547–2552 (2009).
31. Hutchinson, A. B. *et al.* Dissipation in nanocrystalline-diamond nanomechanical resonators. *Appl. Phys. Lett.* **84**, 972–974 (2004).
32. Mohanty, P. *et al.* Intrinsic dissipation in high-frequency micromechanical resonators. *Phys. Rev. B* **66**, 085416 (2002).
33. Evoy, S. *et al.* Temperature-dependent internal friction in silicon nanoelectromechanical systems. *Appl. Phys. Lett.* **77**, 2397–2399 (2000).
34. Chiu, H. Y., Hung, P., Postma, H. W. C. & Bockrath, M. Atomic-scale mass sensing using carbon nanotube resonators. *Nano Lett.* **8**, 4342–4346 (2008).
35. Jensen, K., Kim, K. & Zettl, A. An atomic-resolution nanomechanical mass sensor. *Nature Nanotech.* **3**, 533–537 (2008).
36. Mohiuddin, T. M. G. *et al.* Uniaxial strain in graphene by Raman spectroscopy: G peak splitting, Gruneisen parameters and sample orientation. *Phys. Rev. B* **79**, 205433 (2009).
37. Huang, M. Y. *et al.* Phonon softening and crystallographic orientation of strained graphene studied by Raman spectroscopy. *Proc. Natl Acad. Sci. USA* **106**, 7304–7308 (2009).
38. Blake, P. *et al.* Making graphene visible. *Appl. Phys. Lett.* **91**, 063124 (2007).
39. Ferrari, A. C. *et al.* Raman spectrum of graphene and graphene layers. *Phys. Rev. Lett.* **97**, 187401 (2006).
40. Han, M. Y., Ozyilmaz, B., Zhang, Y. B. & Kim, P. Energy band-gap engineering of graphene nanoribbons. *Phys. Rev. Lett.* **98**, 206805 (2007).

## Acknowledgements

We thank M. Huang for useful discussions, H. Yan for Raman spectroscopy and V. Lee for evaporator setup. This work is supported by the DARPA Center on Nanoscale Science and Technology for Integrated Micro/Nano-Electromechanical Transducers (iMINT, grant no. HR0011-06-1-0048, D.L. Polla, Program Manager), the National Science Foundation (grant no. CHE-0117752), the W. M. Keck Foundation and Microsoft Project Q.

## Author contributions

C.C., S.R. and J.H. designed the experiment. C.C. and W.K. carried out fabrication, S.R. and C.C. performed the experiments and analysed data, and K.B. assisted with the fabrication, measurement and data analysis. I.K. provided assistance with mass sensing. C.C., S.R. and J.H. co-wrote the paper. P.K., H.L.S. and T.F.H. provided materials and equipment. All authors discussed the results and commented on the manuscript.

## Additional information

Supplementary information accompanies this paper at [www.nature.com/naturenanotechnology](http://www.nature.com/naturenanotechnology). Reprints and permission information is available online at <http://npublishing.nature.com/reprintsandpermissions/>. Correspondence and requests for materials should be addressed to J.H.